ADVANCED ENERGY & SUSTAINABILITY RESEARCH
Open Access
www.advenergysustres.com

Toluene-Mediated Morphology Tuning of Diblock Copolymer-Templated Porous Si/Ge/K/C Thin Films for Li-Ion Batteries

*Christian L. Weindl, Kexin Wu, Christian E. Fajman, Zhuijun Xu, Tianle Zheng, Ting Tian, Constantin Harder, Benedikt Sochor, Stephan V. Roth, Thomas F. Fässler, and Peter Müller-Buschbaum**

Amphiphilic diblock copolymer poly(styrene-*b*-ethylene oxide) templating in combination with sol–gel chemistry is utilized to synthesize porous mixed silicon/germanium/potassium/carbon (Si/Ge/K/C) thin films. As a Si/Ge source, the dissolvable Zintl phase $K_{12}Si_{12}Ge_5$ is used. The toluene-mediated morphological changes in the porous mixed Si/Ge/K/C thin films are studied with scanning electron microscopy and grazing incidence small/wide-angle X-Ray scattering. A dichloromethane solvent vapor annealing step is applied to study the additional morphological transformation inside the films. Since Ge and Si are promising anode materials in Li-ion batteries, CR2032 half-cells are manufactured with the porous mixed Si/Ge/K/C thin films and characterized by cyclic voltammograms, cycling, and impedance spectroscopy.

1. Introduction

Within the last two decades, science moved from the micro- to the nanoscale cosmos for the fabrication of novel materials. With this approach, interface areas increased by several orders of magnitude, which added new functions. Moreover, it enabled a miniaturizing of devices, which opened up new applications but also recently gained interest as device components energy consumption shifts more and more into the focus of many applications. As one prominent example, industrial demands appear for nanoengineered sensors, optics, solar cells, and Li-ion batteries in the case of a silicon (Si) fabrication with nanoscale precision.[1–4] Without any doubt, the semiconductor industry sets benchmarks for homogeneous high-precision components for electronic devices in the nanometer regime. However, this is also associated with disadvantages, such as high production costs, highly elaborated fabrication techniques, and high time consumption. Accordingly, other methods appear better suited for the synthesis of porous materials.[5,6] For example, porous materials were successfully achieved by chemical etching, magnesiothermal reduction, or solvothermal synthesis.[7–9] However, bottom-up approaches are better suited for mass production based on printing, spraying, and doctor-blading.[10–12] With these wet chemical deposition techniques, high yields with easy processability and low costs are possible. Among the many different bottom-up approaches, sol–gel synthesis routines were successfully widely used, resulting in a manifold of different porous materials.[13–15] Perhaps, the most widely used porous material is porous titania, which is used in various fields like energy materials, e.g., solar cells, water splitting, or CO_2 reduction.[1,16,17] Importantly, other porous metal oxides also gained attention as promising energy materials like porous iron, tin, and zinc oxides.[18–20] Contrary, studies about porous mixed semimetal films are relatively rare up to

C. L. Weindl, K. Wu, Z. Xu, T. Zheng, T. Tian, C. Harder, P. Müller-Buschbaum
Department of Physics
TUM School of Natural Sciences
Chair for Functional Materials
Technical University of Munich
James-Franck-Str. 1, 85748 Garching, Germany
E-mail: muellerb@ph.tum.de

The ORCID identification number(s) for the author(s) of this article can be found under https://doi.org/10.1002/aesr.202300096.

DOI: 10.1002/aesr.202300096

C. E. Fajman, T. F. Fässler
Department of Chemistry
TUM School of Natural Sciences
Chair of Inorganic Chemistry with Focus on Novel Materials
Technical University of Munich
Lichtenbergstr. 4, 85748 Garching, Germany

C. Harder, B. Sochor, S. V. Roth
Deutsches Elektronen-Synchrotron DESY
Notkestr.85, 22607 Hamburg, Germany

S. V. Roth
Department of Fibre and Polymer Technology
KTH Royal Institute of Technology
Tekinikringen 56-58, SE-100 44 Stockholm, Sweden

P. Müller-Buschbaum
Heinz Maier-Leibnitz Zentrum (MLZ)
Technical University of Munich
Lichtenbergstr. 1, 85748 Garching, Germany

now.[21–23] In this regard, especially Si and germanium (Ge) as anodes in Li-ion batteries (LIBs) show huge benefits such as high theoretical specific capacities (Si: 4200 mAh g^{-1}, Ge: 1600 mAh g^{-1}) and high diffusion coefficient paired with good cycling performance compared to graphite (372 mAh g^{-1}).[3,24] Among the alternatives, Li-metal batteries (3862 mAh g^{-1}) and lithium-titanium-oxide (LTO) batteries (175 mAh g^{-1}) stand out. However, each of these materials faces certain challenges. Li-metal batteries are susceptible to Li dendrite growth, which can compromise their performance, while LTO batteries offer good safety and stability but have a lower specific capacity.[25,26] Additionally, porous anode materials have several advantages, such as efficient ionic and electronic transport or minimized volume expansion effects.[27,28] Furthermore, the incorporation of Ge into the Zintl phase increases solubility and therefore facilitates the fabrication of anode materials out of them. Pure macroporous Ge films were already prepared and applied as anode materials in LIBs.[29,30] Mixed C/Si/Ge and Ge/Sn films have been recently reported as materials for energy storage, but their potential has remained largely unexplored so far.[14,31]

Within this work, we present a novel synthesis route for porous mixed Si/Ge/K/C thin films. A sol–gel synthesis with the amphiphilic diblock copolymer poly(styrene$_{60}$-*b*-ethylene oxide$_{36}$) (PS_{60}-*b*-PEO_{36}) is used to template the dissolved Zintl phase $K_{12}Si_{12}Ge_5$ to gain mesoporous hybrid thin films.[29,30] In general, block copolymer templated sol–gel synthesis was already used to produce anode materials for lithium-ion batteries.[32] For example, Lee et al. reported about sol–gel derived TiO_2/carbon composite coatings for LIBs with high-rate use.[33] Moreover, Yue et al. synthesized polymer-templated mesoporous $Li_4Ti_5O_{12}$ as high-rate and long-life anodes.[34] Furthermore, Jo et al. studied the performance of block copolymer-directed $TiNb_2O_7$ thin films in LIBs.[35] Also, Hohn et al. demonstrated a sol–gel routine to synthesize high-performance anodes with the Zintl phase K_4Ge_9 and the structure-directing agent PS-*b*-PEO.[22] In this work, we demonstrate the tuning of the morphology with a solvent vapor annealing step further to enhance the microphase separation of the hybrid thin film. While previous studies used chloroform (trichloromethane) as an annealing solvent, we selected dichloromethane (DCM) as it provides a higher volatility.[36]

Ten different sample types with varying toluene content and an additional solvent vapor annealing step with DCM are studied. Finally, we also show an application of these Si/Ge/K/C thin films as an anode in Li-ion batteries to emphasize the application potential of the solution-based synthesis routine.

2. Results and Discussion

To acquire information whether the solvent of the Zintl phases ethylenediamine (en) is also a suitable solvent for the two monomers of the diblock copolymer PS_{60}-*b*-PEO_{36}, the relative energy differences (RED) are calculated with the three cohesive energy densities, also known as Hansen solubility parameters (HSPs), for dispersion δ_d, polarity δ_p and hydrogen bonding δ_h, and the interaction radius of the polymer (R_o) (Table S1, Supporting Information). The solubility of the polymer in the solvent can then be evaluated with the HSP distance (R_a) (Equation S1, Supporting Information) by dividing it by R_o from the Supporting Information.[37,38] This results in three regimes related to $RED = R_a/R_0$ (Equation S2, Supporting Information).

The border condition with $RED = 1$ is supposed to be the swelling regime. For RED values smaller than one ($RED < 1$), the solvent well dissolves the polymer. However, chemicals with a RED value above one ($RED > 1$) cannot dissolve the polymer.[38]

From the solution theory, we can estimate that toluene and DCM are suitable solvents for both monomers of the diblock (**Table 1**). As expected, also from the Hildebrand solubility theory, en does not dissolve the polymer at all.[14] It must be mentioned that temperature also plays a significant role in this regard. For example, by increasing the temperature, the HSPs decrease and the solubility of the system changes (Equation (S3)–(S5), Supporting Information).[37] Here, we evidence experimentally that the polymer becomes transparent after reaching a temperature of about 70 °C in pretests. This also matches the findings of the HSP theory that the HSP sphere of the PEO block starts to intersect with the temperature-dependent HSP values of en at elevated temperatures (Figure S1, Supporting Information). This finding can be directly interpreted as a dissolution of the PEO block of the polymer. Unfortunately, increased temperatures negatively influence the Zintl clusters as oxidation followed by precipitation is observed. Therefore, we decided on a solvent tuning route, as en can be blended with tiny amounts of toluene to reach similar effects.[39] The intermixing of both solvents is already done in various other works and does not result in structural changes of the Zintl cluster.[40] No phase separation is observed during the mixing of toluene in ethylenediamine or vice versa. Additionally, an azeotrope is formed at a molar fraction of roughly $X_{en} = 0.38$, which corresponds to a volume fraction of about 28 vol% of en (en28).[41,42] The most interesting area is when the polymer setup gets close to the swelling state with a RED value of 1 (Figure S2, Supporting Information). From these calculations, it can be estimated that volumetric toluene ratios of above 10% should have significantly different morphologies in the sol–gel synthesis than values below 10 vol%. It has to be said that the precursor probably also influences the solubility of the hybrid solution. Since the values for R_o and δ_i are extracted from the literature, a slight deviation can be expected for the experiments.[38,43]

Within this work, we analyze a concentration series of toluene as an additive in the stock solution (constant concentration of precursor to polymer ratio for all toluene variations) and also monitor changes in the thin film morphology when the samples undergo an additional solvent vapor annealing step with

Table 1. Interaction parameter (R_o) with calculated HSP distances (R_a) in $MPa^{1/2}$ and RED values for each polymer/solvent (solv) system used in this work: toluene (tol), ethylenediamine (en), and DCM (Equation (S1) and (S2), Supporting Information).[38,43]

	PS			PEO		
R_o	12.7			10.8		
solv	tol	en	DCM	tol	en	DCM
R_a	3.4	15.2	3.7	9.3	12.1	4.5
RED	0.27	1.20	0.29	0.86	1.12	0.42

dichloromethane (DCM). Both, toluene and DCM are supposed to have an influence on the morphology, which is theoretically predicted from the HSP theory. The sample abbreviations, which apply throughout the whole manuscript, can be extracted from Table 3.

SEM images picture the surface morphology evolution when varying the toluene content after pyrolyzing and washing the thin films (**Figure 1**). Without toluene addition, the images of the en 100 films show a porous morphology with rather random void sizes for both types of films (ref and DCM films, Figure 1a,b, respectively). This finding indicates an inhomogeneous intermixing of the polymer/precursor in the thin film before pyrolysis. Additionally, one can observe an insufficient surface coverage of the silicon wafer at decreased SEM magnifications (Figure S3a,b, Supporting Information). Neither PS nor PEO seem to be nicely dissolved and therefore do not organize in a self-assembled continuous matrix which is in good agreement with the calculations presented before. However, microphase separation occurs and a porous structure can be synthesized. One possible reason can be the partial complexation of the potassium cations during the blending of the diblock with the precursor solution, as the PEO can act like the [2.2.2]-cryptand, which was used in a former study.[14] By adding an overall volume of 5% toluene (en 95 films), a homogenous surface coverage is reached with only minor variations in the film thickness (Figure S3c,d, Supporting Information). In particular, after DCM posttreatment, an increased homogeneity on a large scale is found (Figure S3d, Supporting Information). At an increased magnification, the porous structure contains large worm-like voids and large holes with sizes of about 100–150 nm, which still indicates an incomplete dissolution of the polymer (Figure 1c,d).[44] By increasing the toluene content to 10 vol% (en 90), worm-like voids start to disappear, and spherical-shaped voids dominate the thin films. In the porous structure, small-scale holes in the regime below 20 nm are significantly more prominent in the DCM films than in the ref films (Figure 1e,f). Also, on the large scale, the films are homogeneous and DCM posttreatment does not affect the homogeneity (Figure S3e,f, Supporting Information). No significant structural changes can be evidenced from the SEM images for toluene contents above 15 vol% (Figure 1g–j and Figure S3g–j, Supporting Information). Also, the DCM-treated films do not show any further morphology changes for SEM-accessible magnifications. This behavior exactly matches the estimations of the HSP theory, which proposes a significant increase in homogeneity of the thin films for toluene ratios above 15 vol%. Further, at a ratio of 10 vol% (en 90) an increased film quality is observed, at such ratio likely an intermediate regime is reached. In this regime, PEO is already well dissolved, but the swelling regime of PS still contributes to some larger aggregates in the final thin films (Figure 1e,f).

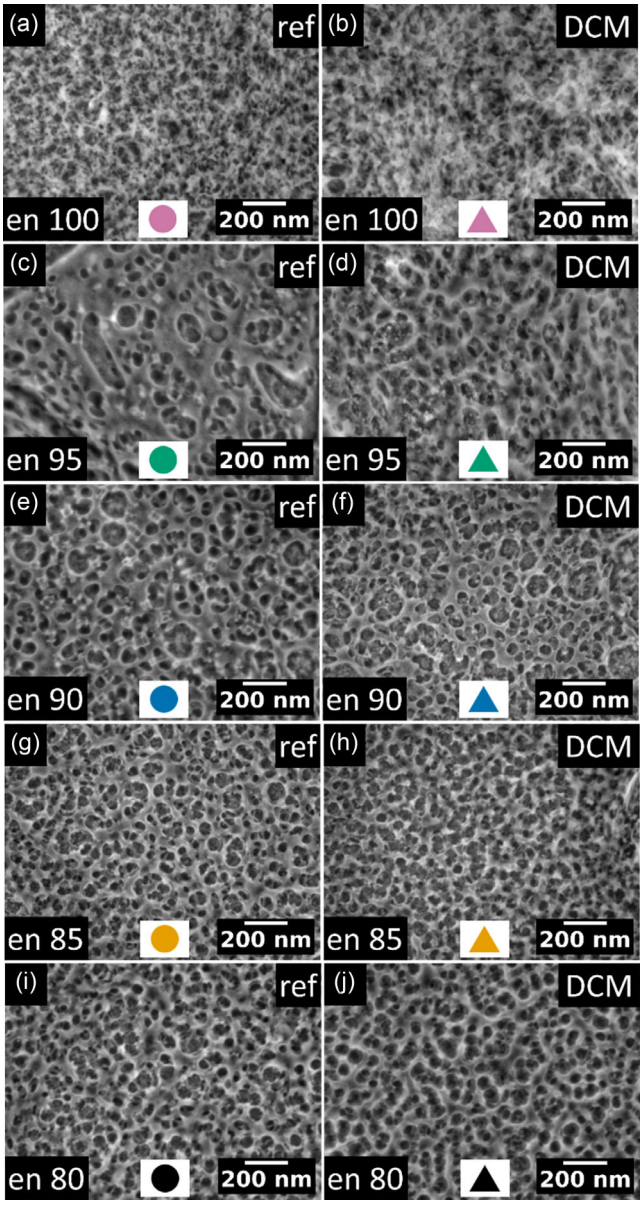

Figure 1. SEM images of thin films without (ref; a, c, e, g, i) and with DCM treatment (DCM; b, d, f, h, j). The corresponding vol% of en in the solution is given in the lower left corner of each image. Colored circles and triangles refer to the color code used in the entire work for the different volumetric en ratios.

In contrast to SEM, which provides surface structure information, grazing incidence small-angle X-Ray scattering (GISAXS) probes the inner film morphology in a noninvasive way.[45] The 2D GISAXS data are shown in Figure S4 (Supporting Information). Comparing the 2D GISAXS data of each column (left = ref, right = DCM) from top to bottom (en 100 to en 80), a significant intensity reduction of the vertical streak at $q_y = 0\,\mathrm{nm}^{-1}$ can be seen. This high-intensity vertical streak represents the resolution limit and scattering in this region arises from large-sized structures, which cannot be resolved in GISAXS. The incomplete coverage of the Si substrate with the hybrid thin film for the spin-coated samples gives rise to such large-scale structures (Figure S4a,b, Supporting Information), whereas the porous morphologies are on a smaller scale and well resolved in the GISAXS measurements. This trend has already been evidenced by the SEM measurements (Figure S3, Supporting Information). Additionally, a second Yoneda peak is clearly seen for $q_z \approx 0.55\,\mathrm{nm}^{-1}$, which starts to appear for 15 vol% toluene (Figure S4g, h, Supporting Information). This peak is attributed to a low-density nanostructure in the thin

film.[15] For clarification, vertical line cuts at $q_y = 0.0\,\mathrm{nm}^{-1}$ are provided (**Figure 2**a,b). Only minor deviations can be detected by comparing the line cuts of the ref and DCM samples with identical toluene ratios (same color in the figure). In addition, another Yoneda peak appears from a volumetric toluene content of 10% on in the case of the ref and DCM films.[46] As already observed with SEM, toluene-mediated swelling of the PEO occurs in the diblock copolymer at such toluene contents.

Both types of films, the ref and DCM films, show this effect, which can be related to increased polymer chain mobility.[44,47] As the dominant monomer in the diblock copolymer is PS, the addition of toluene has a significant effect on the final morphology, as already evidenced in the SEM images and proposed with HSP theory. However, it should be mentioned that this phenomenon is easier to assume in the case of the DCM films, as a more distinct Yoneda peak separation is seen for the DCM film compared to the ref film (blue lines in Figure 2a,b). Additionally, the low-q_z Yoneda peak for the en 80 film exceeds the other Yoneda peak for en 80 of the DCM film. This second peak, which is typically more significant in the DCM films, can be attributed to increased porosity.[48] Explanations for this phenomenon are improved microphase separation and structural reorganization during the SVA process. As a result, there is an increase in the presence of low-density structures, leading to a more substantial Yoneda peak in the low-q_z region. Former experiments showed that the high volatility and optimum HSPs of DCM lead to a complete solvent penetration through the thin film, which was already proven with the similar solvent chloroform in former studies on PS-*b*-PEO (Table 1).[49]

To enable the structural analysis of the thin film's bulk morphology, horizontal line cuts are extracted from the Yoneda position at $q_z \approx 0.6\,\mathrm{nm}^{-1}$. Under the assumption of the local monodisperse approximation (LMA) and the distorted wave-born approximation (DWBA), the data are then modeled.[50,51] Best fits are achieved using three forms and two structure factors. The smallest objects are uncorrelated, which means that the smallest form factor is not modeled with a structure factor.[13] The horizontal line cuts with the corresponding best fits are shown in **Figure 3**a for ref and Figure 3b for the DCM films. The corresponding size distributions of the radii are normalized to the smallest form factor in the thin film (Figure 3c,d), to visualize structural changes of radii above 10 nm. In Figure 3c,d, the black arrow indicates a significant decrease of void radii between en 100 and all other samples. This observation is in good agreement with the findings of the local SEM data (Figure 1). By exchanging 5 vol% of en with tol (sample en 95), the whole film shows a general increase in the radii above 6 nm (Figure 3c). The most significant changes through the solvent series are seen for the largest radii as indicated by the black arrow. A minor variation is also visible for voids with radii between 6 and 20 nm (blue arrow). A further increase in the toluene content then only shows another shift

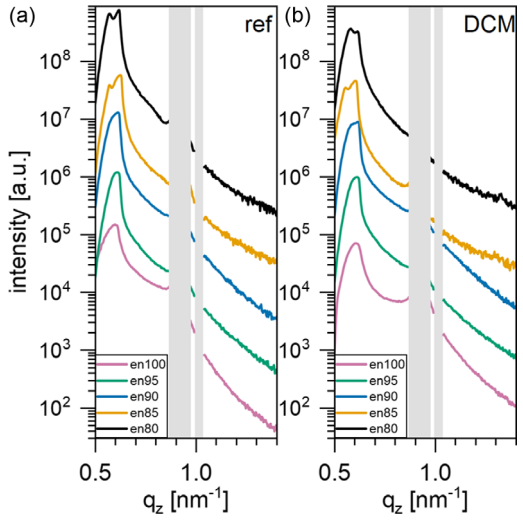

Figure 2. Vertical line cuts of the 2D GISAXS data at $q_y = 0\,\mathrm{nm}^{-1}$ for reference a) and DCM b) thin films with different toluene concentrations. The gray bars denote regions shadowed by the beam stop to avoid oversaturation of the detector and the detector gap located between two detector arrays. The curves are shifted along the *y*-axis for clarity of the presentation.

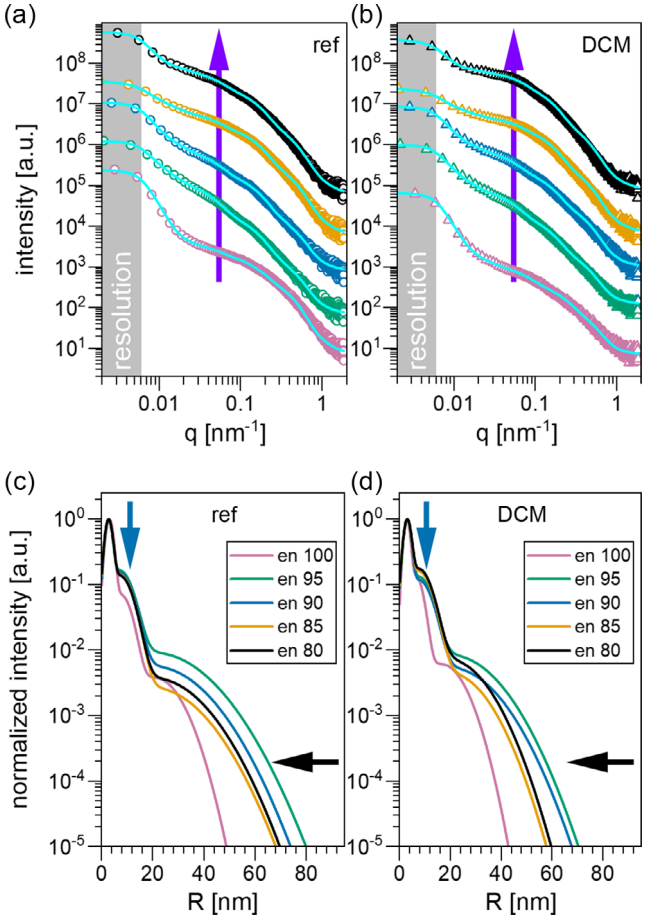

Figure 3. Horizontal line cuts of the 2D GISAXS data with their corresponding best fits (cyan) for ref a) and DCM b) films with different toluene content (color code). The resolution limit of the corresponding measurement is indicated with a gray bar. The purple arrow in both plots indicates structural changes visible in the line cuts. The curves are shifted along the y-axis for clarity of the presentation. From the modeling, the normalized size distributions of the radii for different toluene ratios of ref c) and DCM d) films are shown together with black and blue arrows to indicate the thin film morphology changes.

to smaller radii of the largest structure as a reduction of larger voids, which relates to a reduction of larger holes in the thin film. This finding again matches the SEM images (Figure 1). Thus, increasing the toluene content leads to larger voids in combination with a reduction of large-scale inhomogeneities. At toluene contents of about 15–20 vol%, the amount of larger defects is minimized as both PS and PEO are entirely dissolved. The amount of larger defects generally decreases as the intersection with the radii axis with the distribution curves results in reduced values for the DCM films compared to the ref films (Figure 3c,d). Additionally, DCM seems to be beneficial for controlling the structure sizes in the radii range of 6–20 nm. A possible explanation can be the drying kinetics of the thin films. Toluene has a lower boiling point than en and evaporates first during drying, which freezes then the morphology. This effect may lead to similar sizes in the range of 6–20 nm. Additionally, the dissolution of the polymer before thin film synthesis also plays a dominant role, as we can see aggregate formation at radii above 20 nm. Contrarily, the DCM films undergo an additional SVA step, where both blocks are simultaneously dissolved and polymer chain mobility is maximized. As there is no drying with a temperature treatment, residues of tol/en remain in the thin film. Then, depending on the remaining tol/en ratio in the stock solution, the polymer/hybrid is reassembled in the thin film in a controlled way. Generally, it is apparent that an increasing toluene content shows a higher scattering signal in this range, which is indicated by the blue arrow (Figure 3d).

Overall, the additional solvent vapor annealing step with DCM leads to a minimization of large-void defects for all toluene contents and increases the appearance of structures with radii between 20 and 36 nm for films with toluene contents above 10 vol% (Figure S5, Supporting Information). The modeled structure factors only show differences when toluene is used or not (Figure S6, Supporting Information). By comparing the noncontaining toluene films with each other (en 100), one can see that the DCM leads to a significant decrease in the center-to-center distance D2. This finding supports that the voids with sizes below 15 nm move closer together. Also, the values for D1 are strongly decreased, which suggests an increased order in the film for mean radii sizes of 16.5 nm.

The pretest with the pure precursor with DCM solvent vapor annealing shows the appearance of crystalline Ge (Figure S8a, Supporting Information). The data also indicate remaining amorphous carbon residues from the solvent in the final powder. Accordingly, the influence of toluene and DCM on the film crystalline structures is analyzed with grazing incidence wide-angle X-Ray scattering (GIWAXS). Since the detector has a planar rectangular geometry, the GIWAXS data are reshaped into q space (Figure S7, Supporting Information). Integration into a pseudo-XRD cut enables to extract the position of the characteristic Bragg peaks, such as Ge reflexes (Figure S8b, Supporting Information). Contrary to the only-precursor powder-XRD, the polymer-templated films show reflexes for SiO_2. Oxidation obviously happens for these films with PEO acting as the oxygen source, as no other O_2 source is present. Additionally, the thin films are exposed to air during the GISAXS/GIWAXS measurements. Not all reflexes could be identified. Our primary focus is on analyzing the toluene-dependent Ge crystallinity. The samples without toluene (Figure S7a,b, Supporting Information) clearly show circularly distributed reflexes due to the polycrystallinity. No preferred orientation is seen for the film. The scattering intensity of the reflexes is significantly increased for DCM-treated samples. By increasing the toluene content in the thin films, the reflexes show a decreased intensity for all toluene contents. Thus, the crystallinity correlates with the toluene content for both ref and DCM films.

To further quantify the toluene-dependent intensity distribution, cake cuts of the 2D GIWAXS data are performed in the relevant areas. A bare silicon substrate is measured to subtract the local background of the substrate and a biexponential fit turned out to best describe the Si wafer contribution (Figure S9, Supporting Information). The q-space data are plotted together with the position of Bragg reflexes from potential materials occurring in the films as extracted from the Crystallography Open Database (COD).[52] Crystalline Ge and Si oxides are clearly referenced in the thin films (Figure S8b, Supporting Information).[53–55] Not all peaks could be identified, but all reflexes decrease with an increasing toluene content (Figure S10, Supporting Information). Gaussian fits for amorphous silica/carbon and amorphous silicon are used to describe the local background for a 2θ range between 18° and 36° (Figure S10, Supporting Information). By comparing the ref with the DCM films qualitatively, the intensity of the Ge (111) reflex is increased for all DCM thin films compared to the local amorphous silica/carbon background at around 21°. This observation suggests an increased probability of crystallization or a reduction of amorphous material in the film bulk due to the DCM SVA.

Estimates about crystal sizes are extracted from the FWHM by using the Scherrer equation.[13] Best fits are achieved by using two Gaussian fits in the 2θ-range of Ge. The sharp reflex is attributed to a crystallite size of about 93 nm (Figure S10, Supporting Information). This finding is explained by the absence of toluene, which leads to a decreased intermixing and, therefore, an increased precursor-rich domain formation. As a result, larger crystallites are formed from these domains. This finding also explains the reduced intensities of the SiO_x reflexes, which are significantly decreased for increasing toluene content for ref and DCM films. One has to be cautious to attribute broad reflexes with small intensity to crystallite sizes below one nm, as this could also be identified as an amorphous material. Nevertheless, due to the increased intermixing of the polymer/precursor solution, we assume that there might also be nanocrystals in the lower sub-nm range. However, since this is the subject of controversial discussions in the relevant literature, the authors have restricted themselves to an analysis of crystal sizes below 5 nm. For the ref thin films, no dependency between Ge crystallite size and toluene content can be extracted (**Figure 4**a). Contrarily, the data of the DCM-treated thin films suggest the formation of larger crystallites, which can be attributed to the increased chain mobility of the polymer during the SVA step.

As former studies show that templating the cluster with PS-*b*-PEO leads to carbon residues, this material is promising for binder-free Li-ion batteries.[14] Additionally, the battery performance depends on the stability of the scaffold, which is controllable with the polymer templating mentioned above. As void and scaffold sizes can be engineered with this technique,

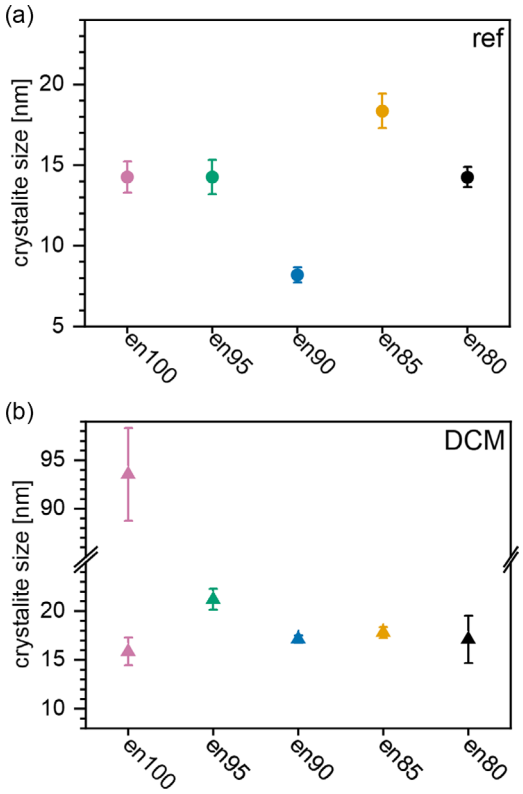

Figure 4. The Scherrer analysis of the pseudo-XRD GIWAXS cuts for ref a) and DCM b) samples with the related color code.

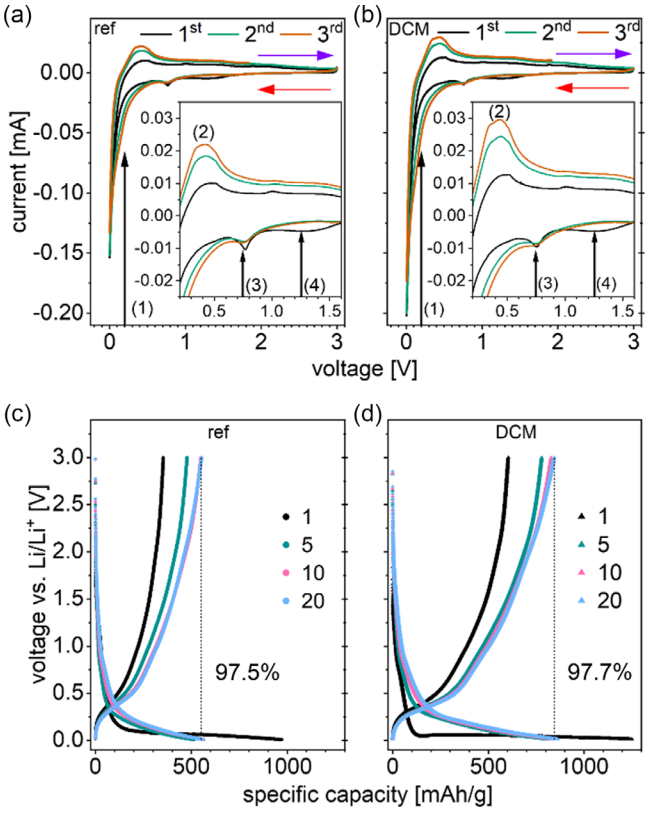

Figure 5. Cyclic voltammetry a,b) and galvanostatic cycling c,d) graphs of ref a,c) and DCM b,d) cells. The names and scales of the ordinates and abscissas are only depicted once but hold for both subplots. In a) and b), the purple and red arrows indicate charge and discharge, respectively. Black arrows with corresponding numbers [(1), (2), (3), (4)] in the inset indicate electrochemical processes in the anode. Galvanostatic cycling curves are shown for the 1st, 5th, 10th, and 20th cycle, respectively. The battery retention for the last cycle is indicated with a dotted line and the corresponding value.

improvements in Li-ion diffusion and electron mobility can be expected. Therefore, we manufacture half cells by drop casting the solution on copper current collectors. As surface-to-volume ratio plays a crucial role, galvanostatic cycling tests are carried out with toluene-free (en 100) films for ref and DCM samples (**Figure 5**a,b). Generally, the observed characteristics are similar to silicon dioxide, with additional peaks for Ge-related processes.[24,56,57] In the first cycle of the cyclic voltammograms, three cathodic peaks are present for the ref and DCM batteries. The first peak is located at 0.02 V, which is attributed to the lithiation of Si and Li_xSi_y alloy formation.[58] For both samples, this peak significantly decreased within the first three cycles for ref and DCM batteries. In contrast, a shoulder grows from the first to the third cycle at a voltage of 0.2 V, which indicates the lithiation of Ge (Figure 5a,b (1)).[24] The reduction of GeO_2 over a lithiation process to Ge amplifies this behavior.[59] The cathodic peak at around 0.8 V is characteristic of the reduction of Si oxides. As the peak begins to vanish and forms a plateau for the subsequent cycles, we suggest an irreversible lithiation reaction. Additionally, a broad peak is visible at voltages of about 1.3 V (4), which is assigned to the formation of the solid-electrolyte interface (SEI) with the FEC additive at the initial cycle.[60] It vanishes as the formation of the SEI is completed after the first cycle. On the oxidation (charge), a superposition of peaks starts to arise in the range between 0.4 and 0.5 V (2), which increases within the first three cycles. This superposition can be related to the delithiation reaction of Li_xSi_y to Si as well as the reaction of Li_xGe_y to Ge.[58,59] As the oxidation and reduction peaks of Si and Ge (1, 2) show no change in the peak position, the material is well suited as an anode. The decrease at 0.02 V suggests a loss of amorphous Si in the anode. Tiny peaks are also visible at around 1.0 V, where the reoxidation of Ge/Li_2O to GeO is supposed to happen and get less pronounced in the 2nd and 3rd cycle.[61] The last reaction occurs at around 1.8 V, which is attributed to an irreversible process as the peak intensity decays with an increasing cycle number.

The discharge curves show a good agreement with the findings from the cyclic voltammograms, as the discharge capacity is dominated by electrochemical reactions below 0.5 V, which is the range where the lithiation of Ge and Si happens (Figure 5c,d).[61,62] Fluctuations of the corresponding slopes are attributed to irreversible reactions of Si/Ge oxides and the formation of the solid-electrolyte interface (SEI). The discharge plateau formation at a voltage range of 0.8 V (3) is assigned to the reversible insertion reaction of SiO_2 with lithium.[63] In the charging curves, there is a significant change in the slope characteristics at 0.4 V, which is assigned to the reoxidation of

Li_xGe and is in complete agreement with the CV analysis (2). Finally, a high retention rate for both ref and DCM anodes of about 97% is achieved during the cycling process. Thus, we can summarize that the half-cell stabilizes within the first 15 cycles as Si and Ge oxides deliver additional Si and Ge for the following lithiation processes in an irreversible electrochemical process. The increasing specific capacity within the first cycles and the following stabilization of the ref ($\approx$550 mAh g^{-1}) and DCM ($\approx$800 mAh g^{-1}) is also evidenced in the charge/discharge with the coulombic efficiency plots and can be attributed to material activation and sufficient infiltration of the electrolyte (Figure S11, Supporting Information).[64] As the DCM treatment does not deliver any additional peaks in the CV analysis, the increased specific capacity can be ascribed to the morphology change during reassembly in the SVA process, evidenced in the GISAXS analysis. Generally, the performance within the first 20 cycles is reduced compared to other works on porous Si anodes, which are in the range of 1000–3000 mAh g^{-1}.[3] However, compared to their corresponding synthesis techniques, the easy morphological and compositional tunability of the polymer-templated Zintl cluster anodes are a promising high-yield alternative when applied to printing or spraying, which is restricted to chemical synthesis routines.

The DCM anode's increased performance can have several reasons, like an enhanced morphology or more pronounced reversible electrochemical processes. Another crucial parameter is the lithiation kinetics during charge and discharge. Therefore, electrochemical impedance spectroscopy data are collected (Figure S12, Supporting Information). Data evaluation leads to the charge-transfer resistance R_{ct} values summarized in **Table 2**.

Generally, charge transfer resistances are decreased for DCM-treated anodes, which can originate from several reasons. As the cell chemistry for both types is nearly identical, this performance boost can be attributed to the additional DCM treatment. Follow-up parameters still originate also based on this major difference. As we investigated with GISAXS, there is a beneficial morphological change in the thin films. Increased homogeneity and the reduction of larger aggregates are evidenced in the GISAXS analysis. Additionally, an increased amount of crystalline Ge can have a beneficial impact on R_{ct}. Contrary, it is not entirely proven which effect plays the dominant role in the performance boost in the elated batteries. After the cycling, charge transfer resistances rise $\approx$59% for the DCM and $\approx$33% for the ref batteries. This degradation can be referred to as the formation of the SEI, Li-trapping, and volume expansion effects during lithiation.[65] However, R_{ct} values are still significantly decreased by comparing it with Si and Ge nanoparticles, which are about 700 and 600 Ω, respectively.[59,66]

Table 2. Charge transfer (R_{ct}) and series resistance (R_0) values extracted from electrochemical impedance spectroscopy measurements for ref and DCM anodes before and after galvanostatic cycling.

	R_0 [Ω] Before cycling	R_{ct} [Ω] Before cycling	R_0 [Ω] After cycling	R_{ct} [Ω] After cycling
ref	1.43 ± 0.06	106.80 ± 3.12	0.94 ± 0.07	142.45 ± 4.18
DCM	1.41 ± 0.02	79.49 ± 0.99	1.04 ± 0.05	126.50 ± 1.97

3. Conclusion

We demonstrate a sol–gel routine with PS_{60}-*b*-PEO_{36} and the en soluble Zintl phase $K_{12}Si_{12}Ge_5$ to synthesize porous Si/Ge/K/C thin films with controllable morphology. Based on SEM, we show that toluene plays a significant role in improving the thin film surface coverage and homogeneity by minimizing the amount of larger aggregates in the bulk. Furthermore, with GISAXS, the structural changes in the bulk are determined with statistical relevance. Additionally, the scattering data for films with high toluene content show the appearance of low-density q-regions in the vertical line cuts, which relate to small-scale porosity in the thin film. The usage of an additional solvent vapor annealing step with DCM further improves this. GIWAXS shows that the toluene content is not directly linked with the size of the Ge nanocrystallites. However, a reduction of amorphous material combined with slightly increased crystallite size is caused by the DCM treatment. The very first use of this synthesis route for the application in Li-ion batteries already shows promising results. The cycling performance with the DCM-treated anodes outperforms the reference anodes. The cyclic voltammetry data show typical SiO_2 behavior with additional Ge-based electrochemical processes.

Since the properties of the polymer and precursor can be adjusted according to needs, the presented synthesis route is by far not limited to an application in Li-ion batteries. Also, applications in other areas are highly recommended, as mass production with printing techniques is conceivable.

4. Experimental Section

General: All thin film synthesis procedures were performed under standard Schlenk line or glovebox techniques under an oxygen and water-free, inert gas atmosphere. Manufacturing steps for coin cell assembly were performed in an argon glovebox. Ethylenediamine was refluxed over calcium hydride for 72 h prior to use. All other solvents were purified by an MBraun Grubbs apparatus, degassed by three cycles of freeze pump thaw, and stored over a 3 Å molecular sieve. The starting material $K_{12}Si_{12}Ge_5$ was prepared according to the literature.[14]

Synthesis of $K_{12}Si_{12}Ge_5$: With tuned literature values of the Zintl phase synthesis, the Si/Ge precursor was produced as described before.[14,30] The purity of the phase was confirmed with powder PXRD (Figure S13, Supporting Information).

Thin Film Synthesis: The precursor $K_{12}Si_{12}Ge_5$ (35 mg, 30 µmol) was dissolved in 1 mL water-free ethylenediamine (en) with a concentration of 35 mg mL^{-1} and stirred for 3 days for optimal phase dissolution. The precursor solution was filtered with a 0.7 µm glass fiber filter to remove any undissolved material. Due to the lower likelihood of Si dissolution in en, the Si/Ge ratio was effectively decreased from 12/5 of the initial phase to a measured value of 7.2/5 as probed with energy-dispersive X-Ray spectroscopy. Additionally, the Zintl phase is composed of four and nine atomic clusters in the ratio 1 to 2. Therefore, the phase can also be written as $[K_4Si_{2.8}Ge_{1.2}]_2$*$[K_4Si_{6.4}Ge_{2.6}]$. Generally, the four atomic clusters show weak to no solubility in en. Consequently, an atomic K/Si ratio of 1/1.6 can be assumed. However, the measured amount of K in the film is about 1/2. Reasons for this can be related to the pyrolysis and subsequent washing process. The amphiphilic diblock-copolymer poly(styrene-*b*-ethylene oxide) (PS-*b*-PEO) (20 mg, 0.2 µmol) (Polymer Source Inc. polydispersity = 1.09, M_n(PS) = 60.0 kg mol^{-1}, M_n(PEO) = 36.0 kg mol^{-1}) was used as the organic template of the thin films. With a concentration of 20 mg mL^{-1}, the stock solutions of polymer/toluene and polymer/en were stirred for one day (500 rpm).

After that, a concentration series with different volumes of en and toluene was prepared from the two stock solutions by a constant ratio of precursor/polymer, as described in **Table 3**.

Subsequently, solutions with different en/toluene ratios were intermixed with the precursor solution. After mixing for 2 h, 20 µL of the polymer/precursor solution was statically spin-coated (1000 rpm, 30 s) on precleaned Si substrates (10 mm × 15 mm), which were cut out of full size wafers (Si-Mat, p-doped, <100>, diameter = 100 mm, 0.005–0.02 Ω cm, thickness = 525 ± 25 µm). The substrates were precleaned with an alkaline bath, and treated with oxygen plasma to gain a deprotonated surface. Subsequently, half of the hybrid thin films were stored for 12 h in a sealed container under the presence of dichloromethane (DCM), whereas the used amount of solvent here was 10 µL/substrate. Meanwhile, the other half of the thin films remained in the glove box without any further treatment and therefore are named reference samples (ref) (**Scheme 1**). Subsequently, a pyrolysis step up to 500 °C was performed to evaporate the organic template and establish the mesoporous hybrid thin film. A further increase to 600 °C for 10 min led to an increased crystallinity of the mesoporous hybrid thin films. Subsequent cleaning steps (30 min each) with dimethyl sulfoxide (DMSO) and tetrahydrofuran (THF) removed the remaining organic residues.[14]

Thin Film Battery Anodes: Circular copper sheets with a diameter of 14 mm (99.9%, 100 µm) were punched out mechanically for the anodes. Cleaning steps stayed the same without applying the oxygen plasma as copper heavily oxidates. After drop-casting of 20 µL, the samples were treated equally compared to the Si-substrate thin films. Additionally, the liquid electrolyte and coin cell (CR2032) manufacturing was prepared in an argon glove box to avoid lithium-nitrogen interactions. An amount of 80 µL of the mixed electrolyte was used, which consists of a blend of 1.0 M $LiPF_6$ in ethylene carbonate (EC))—dimethyl carbonate (DMC)–diethyl carbonate (DEC) (1:1:1 vol%) with 5 wt% of fluoroethylene carbonate (FEC) (all purchased from Zhangjiagang Guotai-Huarong Commercial New Material Co., Ltd.). Polypropylene (PP)/polyethylene (PE) separators from Celgard with a thickness of 16 µm were used in the half cells. Pure lithium (Li) foil (99.9%, 500 µm, Dongguan Shanshan Battery Materials Co., Ltd) with a diameter of 16 mm was used as the counter electrode, with a stainless steel plate (500 µm) and a spring between the current collector and the case. The cell stack (lower case/copper+hybrid material/separator/Li-foil/current collector/spring/upper case) was finalized by applying a pressure of 1000 PSI in a specially designed coin cell press to seal the coin case and provide good contact between the layers.

Scanning Electron Microscopy (SEM): Surface analysis was performed with a scanning electron microscope from Zeiss (Gemini NVision 40). With working distances of about 4 mm and a voltage of 5 kV, images with magnifications of 10 k× and 80 k× were made. Adjusting brightness and contrast was then done before inserting the scale bar with a self-written Python script with the libraries of numpy, scipy, matplotlib, and scikit-image.[67–70]

Energy-Dispersive X-Ray Spectroscopy: The electron source utilized in this study was a Zeiss EVO MA10 scanning electron microscope. The acceleration voltage was adjusted to 20 kV. Compositional information was acquired using a Bruker X Flash 6–30 detector. The obtained data were evaluated through the application of Bayes deconvolution and Phi-Rho-Z quantification methods.

Table 3. Sample code of the solution series with different volume percentages of ethylenediamine and toluene in the thin films. The abbreviation for solvent vapor annealing with dichloromethane is DCM and for the reference samples, which did not undergo the SVA step, is ref.

Sample code	en 100	en95	en90	en85	en80
vol% en	100	95	90	85	80
vol% tol	0	5	10	15	20
SVA		DCM	reference		ref

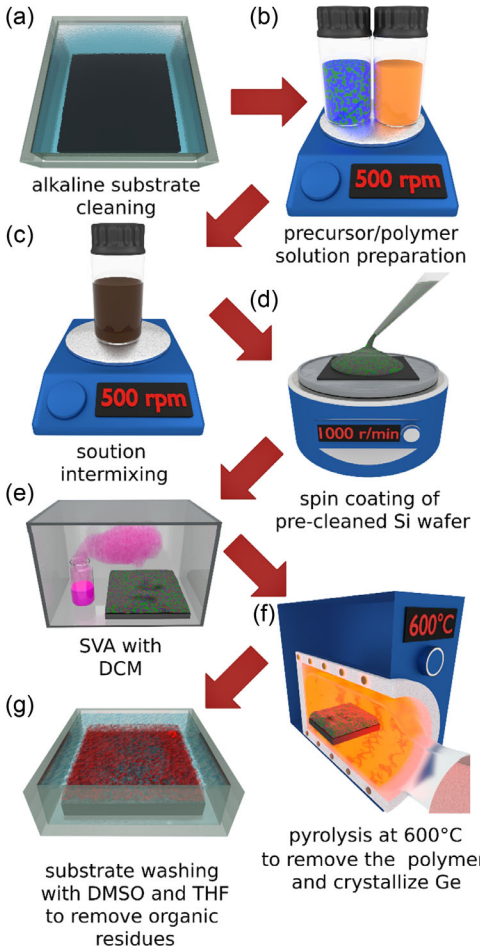

Scheme 1. Thin film synthesis of the porous Si/Ge/K/C thin films comprising steps of a) alkaline substrate cleaning, b) precursor/polymer solution preparation, c) solution intermixing, d) spin coating on precleaned Si wafers, e) SVA with DCM, f) pyrolysis at 600 °C to remove the polymer and crystallize Ge, and g) substrate washing with DMSO and THF to remove organic residues as described in the text.

Grazing Incidence Small-/Wide-Angle X-Ray Scattering (GISAXS/GIWAXS): X-Ray scattering experiments were conducted at the Deutsches Elektronen Synchrotron (DESY) facility in Hamburg. All the samples were measured at the beamline P03 of PETRA III with an incident angle of $\alpha_i = 0.4°$ and an X-Ray wavelength of 0.95 Å.[71,72] The sample-detector-distance (SDD) was set to 4169.0 mm for GISAXS. The 2D scattering data were collected with a Pilatus 2M (Dectris Ltd.) with 1475 × 1679 pixels and a pixel size of (172 × 172) µm^2. Beam stops were set to the direct and specular beam position to avoid oversaturation of the corresponding pixels and detector damage. To increase the signal-to-noise ratio, 20 individual frames of each sample were summed up. Horizontal and vertical line cuts were performed at the corresponding Yoneda peak positions with the software DPDAK.[73] While for GIWAXS, the angle and wavelength remained identical to the GISAXS measurements, the SDD was set to 300 mm to observe the high-q region. The detector used for GIWAXS was the Lambda 9M (X-Spectrum) with 4227 × 2490 pixels and a pixel size of (55 × 55) µm. Image processing steps such as geometry calculations, intensity corrections for path attenuation, detector absorption, photon polarization, q-space transformations, and solid angle corrections were done with the Python package INSIGHT.[74,75] To get information about the crystallinity of the thin films, cake cuts were

performed with $\chi = [0°, 35°]$ and $q_r = [0.3\ Å^{-1}, 4\ Å^{-1}]$. The Ge (111) peak was used to correct the SDD. Finally, the q-space was recalculated to the corresponding 2theta angles of the K_α line of copper (pseudo-XRD) and could be easily compared to crystal data from the Crystallography Open Database (COD).[52] Already published crystal phases were used to simulate the XRD pattern with VESTA for comparison.[76]

Powder XRD (PXRD): The pyrolyzed and washed precursor was sealed in glass capillaries (MARK-Kapillaren, outer diameter: 0.3 mm, wall thickness: 0.01 mm, Müller & Müller OHG) and measured in Debye–Scherrer geometry with a Stoe STADIP diffractometer [Ge(111) monochromator; Cu K_α radiation], including a linear position-sensitive detector (Mythen). The collected data were compared with generated diffractograms (VESTA) from the COD.[14,76]

Galvanostatic Cycling: Cycling tests were performed at room temperature (25 °C) in the range of 0.005 V–3.0 V (V vs Li/Li^+) with the model CT-ZWJ-4S-T-1U from NEWARE. The current used was related to 0.1 C of the half cell. The mass of the porous hybrid thin film was determined by balancing the copper anodes three times before the thin film deposition and after the final washing step. The mass was estimated by several balancing steps of each anode and a subsequent calculation of the corresponding mean values.

Cyclic Voltammetry (CV) and Electrochemical Impedance Spectroscopy: The CV and impedance measurements were done with the VMP-300 from BioLogic SAS. For the CV analysis, the applied potential is $dE/dt = 0.1\ mV\ s^{-1}$. With this parameter, the cycling was finished in 25 h with a repeat number of two. The CV potential range was chosen between 0.005 and 3 V. The impedance data were recorded with the same device, a frequency range between 0.1 Hz and 1 MHz, and an excitation amplitude of 10 mV. The collected data were then transferred into the Nyquist plot, which displays the real versus the imaginary part of the impedance.

Supporting Information

Supporting Information is available from the Wiley Online Library or from the author.

Acknowledgements

The authors thank Deutsche Forschungsgemeinschaft (DFG) for financial support via the International Research Training Group 2022 the Alberta/Technical University of Munich International Graduate School for Environmentally Responsible Functional Materials (ATUMS) and under Germany's Excellence Strategy – EXC 2089/1 – 390776260 (e-conversion) as well as from TUM.solar in the context of the Bavarian Collaborative Research Project Solar Technologies Go Hybrid (SolTech). T.T. acknowledges the China Scholarship Council (CSC) funding. The authors thank Prof. Alexander Holleitner and Claudia Paulus for providing access to the scanning electron microscope. Parts of this research were carried out at the light source PETRA III at DESY, a member of the Helmholtz Association (HGF).

Open Access funding enabled and organized by Projekt DEAL.

Conflict of Interest

The authors declare no conflict of interest.

Author Contributions

The manuscript was written through contributions of all authors. All authors have given approval to the final version of the manuscript.

Data Availability Statement

The data that support the findings of this study are available from the corresponding author upon reasonable request.

Keywords

diblock copolymers, Li-ion batteries, porous films, Si/Ge/K/C, solvent vapor annealing

Received: June 1, 2023
Revised: August 10, 2023
Published online: August 30, 2023

[1] J. Shao, S. Yang, L. Lei, Q. Cao, Y. Yu, Y. Liu, *Chem. Mater.* **2016**, *28*, 7134.
[2] A. Haroun, X. Le, S. Gao, B. Dong, T. He, Z. Zhang, F. Wen, S. Xu, C. Lee, *Nano Ex.* **2021**, *2*, 22005.
[3] M. Ge, X. Fang, J. Rong, C. Zhou, *Nanotechnology* **2013**, *24*, 422001.
[4] P. Dombi, Z. Pápa, J. Vogelsang, S. V. Yalunin, M. Sivis, G. Herink, S. Schäfer, P. Groß, C. Ropers, C. Lienau, *Rev. Mod. Phys.* **2020**, *92*, 025003.
[5] J. Kim, O. Wilhelm, S. E. Pratsinis, *J. Am. Ceram. Soc.* **2001**, *84*, 2802.
[6] N. Li, W. Chen, L. Song, R. Guo, M. A. Scheel, D. Yang, V. Körstgens, M. Schwartzkopf, S. V. Roth, P. Müller-Buschbaum, *ACS Appl. Mater. Interfaces* **2020**, *12*, 57627.
[7] S. A. Ajeel, K. A. Sukkar, N. K. Zedin, *Mater. Today Proc.* ***2021***, *42*, 1966.
[8] H. Li, H. Li, Y. Lai, Z. Yang, Q. Yang, Y. Liu, Z. Zheng, Y. Liu, Y. Sun, B. Zhong, Z. Wu, X. Guo, *Adv. Energy Mater.* **2022**, *12*, 2102181.
[9] L. Lin, X. Xu, C. Chu, M. K. Majeed, J. Yang, *Angew. Chem.* **2016**, *128*, 14269.
[10] M. Zhang, J. Li, C. Sun, Z. Wang, Y. Li, D. Zhang, *J. Alloys Compd.* **2023**, *932*, 167687.
[11] B. Wang, J. Jin, Z. Wen, *Chem. Eng. J.* **2019**, *360*, 1301.
[12] I. P. Gordon, W. Xu, S. Randak, T. R. Jow, N. P. Stadie, *Chem. Mater.* **2023**, *35*, 549.
[13] J. E. Heger, W. Chen, S. Yin, N. Li, V. Körstgens, C. J. Brett, W. Ohm, S. V. Roth, P. Müller-Buschbaum, *Adv. Funct. Mater.* **2022**, *32*, 2113080.
[14] C. L. Weindl, C. E. Fajman, M. A. Giebel, K. S. Wienhold, S. Yin, T. Tian, C. Geiger, L. P. Kreuzer, M. Schwartzkopf, S. V. Roth, T. F. Fässler, P. Müller-Buschbaum, *ACS Appl. Nano Mater.* **2022**, *5*, 7278.
[15] S. Yin, T. Tian, K. S. Wienhold, C. L. Weindl, R. Guo, M. Schwartzkopf, S. V. Roth, P. Müller-Buschbaum, *Adv. Mater. Interfaces* **2020**, *7*, 2001002.
[16] T. Feng, Q. Ren, Z. Song, C. Feng, P. Zhou, M. Wang, Q. Zhang, L. Wang, *Ceram. Int.* **2023**, *49*, 14587.
[17] Q.-Y. Li, S.-D. Han, J.-G. Liu, L.-Y. Sun, Y.-L. Wang, Q. Wei, S.-P. Cui, *Colloids Surf., A* **2023**, *658*, 130707.
[18] S. Yin, W. Cao, Q. Ji, Y. Cheng, L. Song, N. Li, C. L. Weindl, M. Schwartzkopf, S. V. Roth, P. Müller-Buschbaum, *Adv. Mater. Interfaces* **2021**, *8*, 2100141.
[19] M. Derouiche, R. Salhi, S. Baklouti, *J. Radiat. Res. Appl. Sci.* **2023**, *16*, 100497.
[20] M. Brella, A. Taabouche, B. Gharbi, R. Gheriani, Y. Bouachiba, A. Bouabellou, H. Serrar, S. Touil, K. Laggoune, M. Boudissa, *Semiconductors* **2022**, *56*, 234.
[21] W. Zhang, J. Li, P. Guan, C. Lv, C. Yang, N. Han, X. Wang, G. Song, Z. Peng, *J. Alloys Compd.* **2020**, *835*, 155135.

[22] N. Hohn, X. Wang, M. A. Giebel, S. Yin, D. Müller, A. E. Hetzenecker, L. Bießmann, L. P. Kreuzer, G. E. Möhl, H. Yu, J. G. C. Veinot, T. F. Fässler, Y.-J. Cheng, P. Müller-Buschbaum, *ACS Appl. Mater. Interfaces* **2020**, *12*, 47002.
[23] J. Hwang, C. Jo, M. G. Kim, J. Chun, E. Lim, S. Kim, S. Jeong, Y. Kim, J. Lee, *ACS Nano* **2015**, *9*, 5299.
[24] B. Laforge, L. Levan-Jodin, R. Salot, A. Billard, *J. Electrochem. Soc.* **2008**, *155*, A181.
[25] C. Fang, X. Wang, Y. S. Meng, *Trends Chem.* **2019**, *1*, 152.
[26] H. Zhang, Y. Yang, H. Xu, L. Wang, X. Lu, X. He, *InfoMat* **2022**, *4*, e12228.
[27] F. Dai, R. Yi, H. Yang, Y. Zhao, L. Luo, M. L. Gordin, H. Sohn, S. Chen, C. Wang, S. Zhang, D. Wang, *ACS Appl. Mater. Interfaces* **2019**, *11*, 13257.
[28] D. T. Ngo, H. T. T. Le, C. Kim, J.-Y. Lee, J. G. Fisher, I.-D. Kim, C.-J. Park, *Energy Environ. Sci.* **2015**, *8*, 3577.
[29] S. Geier, R. Jung, K. Peters, H. A. Gasteiger, D. Fattakhova-Rohlfing, T. F. Fässler, *Sustain. Energy Fuels* **2018**, *2*, 85.
[30] M. M. Bentlohner, M. Waibel, P. Zeller, K. Sarkar, P. Müller-Buschbaum, D. Fattakhova-Rohlfing, T. F. Fässler, *Angew. Chem.* **2016**, *128*, 2487.
[31] S. Geier, T. Kratky, S. Günther, T. F. Fässler, *Z. Anorg. Allg. Chem.* **2022**, *648*, e202100362.
[32] M. C. Orilall, U. Wiesner, *Chem. Soc. Rev.* **2011**, *40*, 520.
[33] J. Lee, Y. S. Jung, S. C. Warren, M. Kamperman, S. M. Oh, F. J. DiSalvo, U. Wiesner, *Macromol. Chem. Phys.* **2011**, *212*, 383.
[34] J. Yue, C. Suchomski, T. Brezesinski, B. M. Smarsly, *ChemNanoMat* **2015**, *1*, 415.
[35] C. Jo, Y. Kim, J. Hwang, J. Shim, J. Chun, J. Lee, *Chem. Mater.* **2014**, *26*, 3508.
[36] C. P. Glagola, L. M. Miceli, M. A. Milchak, E. H. Halle, J. L. Logan, *Langmuir* **2012**, *28*, 5048.
[37] C. M. Hansen, A. Beerbower, *Kirk-Othmer Encycl. Chem. Technol.* **1971**, *2*, 889.
[38] C. M. Hansen, *Hansen Solubility Parameters: A User's Handbook*, 2nd ed., CRC Press, Boca Raton **2007**.
[39] M. D. de los Ríos, E. Hernández Ramos, *SN Appl. Sci.* **2020**, *2*, 676.
[40] R. Hauptmann, T. F. Fässler, *Z. Kristallogr. NCS* **2003**, *218*, 493.
[41] S. K. Chaudhari, S. S. Katti, *Indian J. Technol.* **1985**, *23*, 74.
[42] J. Gmehling, J. Menke, J. Krafczyk, K. Fischer (Eds), *Azeotropic Data*, Weinheim, New York, Basel, Cambridge, Tokyo **1995**.
[43] C. Özdemir, A. Güner, *Eur. Polym. J.* **2007**, *43*, 3068.
[44] J. Peng, Y. Han, W. Knoll, D. H. Kim, *Macromol. Rapid Commun.* **2007**, *28*, 1422.
[45] P. Müller-Buschbaum, *Eur. Polym. J.* **2016**, *81*, 470.
[46] Y. Yoneda, *Phys. Rev.* **1963**, *131*, 2010.
[47] C. Sinturel, M. Vayer, M. Morris, M. A. Hillmyer, *Macromolecules* **2013**, *46*, 5399.
[48] A. Alvarez-Fernandez, B. Reid, M. J. Fornerod, A. Taylor, G. Divitini, S. Guldin, *ACS Appl. Mater. Interfaces* **2020**, *12*, 5195.
[49] T. Ghoshal, J. D. Holmes, M. A. Morris, *Sci. Rep.* **2018**, *8*, 7252.
[50] R. Lazzari, *J. Appl. Crystallogr.* **2002**, *35*, 406.
[51] M. Newville, T. Stensitzki, D. B. Allen, M. Rawlik, A. Ingargiola, A. Nelson, *Astrophys. Source Code Library* **2016**, ascl:1606.014.
[52] S. Gražulis, D. Chateigner, R. T. Downs, A. F. T. Yokochi, M. Quirós, L. Lutterotti, E. Manakova, J. Butkus, P. Moeck, A. Le Bail, *J. Appl. Crystallogr.* **2009**, *42*, 726.
[53] A. S. Cooper, *Acta. Cryst.* **1962**, *15*, 578.
[54] S. Endo, T. Akai, Y. Akahama, M. Wakatsuki, T. Nakamura, Y. Tomii, K. Koto, Y. Ito, M. Tokonami, *Phys. Chem. Minerals.* **1986**, *13*, 146.
[55] K. Kihara, T. Matsumoto, M. Imamura, *Z. Kristallogr. - Cryst. Mater.* **1986**, *177*, 27.
[56] B. Guo, J. Shu, Z. Wang, H. Yang, L. Shi, Y. Liu, L. Chen, *Electrochem. Commun.* **2008**, *10*, 1876.
[57] Q. Sun, B. Zhang, Z.-W. Fu, *Appl. Surf. Sci.* **2008**, *254*, 3774.
[58] A. Mukanova, A. Nurpeissova, S.-S. Kim, M. Myronov, Z. Bakenov, *ChemistryOpen* **2018**, *7*, 92.
[59] S. Yan, H. Song, S. Lin, H. Wu, Y. Shi, J. Yao, *Adv. Funct. Mater.* **2019**, *29*, 1807946.
[60] G. Zhu, S. Yang, Y. Wang, Q. Qu, H. Zheng, *RSC Adv.* **2018**, *9*, 435.
[61] L. Zeng, X. Huang, X. Chen, C. Zheng, Q. Qian, Q. Chen, M. Wei, *ACS Appl. Mater. Interfaces* **2016**, *8*, 232.
[62] S.-H. Ng, J. Wang, D. Wexler, K. Konstantinov, Z.-P. Guo, H.-K. Liu, *Angew. Chem., Int. Ed.* **2006**, *45*, 6896.
[63] Z. Bai, W. Tu, J. Zhu, J. Li, Z. Deng, D. Li, H. Tang, *Polymers* **2019**, *11*, 576.
[64] B. Huang, B. Chu, T. Huang, A. Yu, *Molecules* **2021**, *26*, 1536.
[65] D. Rehnlund, Z. Wang, L. Nyholm, *Adv. Mater.* **2022**, *34*, e2108827.
[66] Y. Zhang, K. Li, P. Ji, D. Chen, J. Zeng, Y. Sun, P. Zhang, J. Zhao, *J. Mater. Sci.* **2017**, *52*, 3630.
[67] C. R. Harris, K. J. Millman, S. J. van der Walt, R. Gommers, P. Virtanen, D. Cournapeau, E. Wieser, J. Taylor, S. Berg, N. J. Smith, R. Kern, M. Picus, S. Hoyer, M. H. van Kerkwijk, M. Brett, A. Haldane, J. F. Del Río, M. Wiebe, P. Peterson, P. Gérard-Marchant, K. Sheppard, T. Reddy, W. Weckesser, H. Abbasi, C. Gohlke, T. E. Oliphant, *Nature* **2020**, *585*, 357.
[68] J. D. Hunter, *Comput. Sci. Eng.* **2007**, *9*, 90.
[69] P. Virtanen, R. Gommers, T. E. Oliphant, M. Haberland, T. Reddy, D. Cournapeau, E. Burovski, P. Peterson, W. Weckesser, J. Bright, S. J. van der Walt, M. Brett, J. Wilson, K. J. Millman, N. Mayorov, A. R. J. Nelson, E. Jones, R. Kern, E. Larson, C. J. Carey, İ. Polat, Y. Feng, E. W. Moore, J. VanderPlas, D. Laxalde, J. Perktold, R. Cimrman, I. Henriksen, E. A. Quintero, C. R. Harris, et al., *Nat. Methods* **2020**, *17*, 261.
[70] S. van der Walt, J. L. Schönberger, J. Nunez-Iglesias, F. Boulogne, J. D. Warner, N. Yager, E. Gouillart, T. Yu, *PeerJ* **2014**, *2*, e453.
[71] A. Buffet, A. Rothkirch, R. Döhrmann, V. Körstgens, M. M. Abul Kashem, J. Perlich, G. Herzog, M. Schwartzkopf, R. Gehrke, P. Müller-Buschbaum, S. V. Roth, *J. Synchrotron Radiat.* **2012**, *19*, 647.
[72] K. P. Giannakopoulos, S. Roth, M. Burghammer, C. Fellous, D. Richard, D. Dutartre, *J. Appl. Phys.* **2003**, *93*, 259.
[73] G. Benecke, W. Wagermaier, C. Li, M. Schwartzkopf, G. Flucke, R. Hoerth, I. Zizak, M. Burghammer, E. Metwalli, P. Müller-Buschbaum, M. Trebbin, S. Förster, O. Paris, S. V. Roth, P. Fratzl, *J. Appl. Crystallogr.* **2014**, *47*, 1797.
[74] M. A. Reus, L. K. Reb, A. F. Weinzierl, C. L. Weindl, R. Guo, T. Xiao, M. Schwartzkopf, A. Chumakov, S. V. Roth, P. Müller-Buschbaum, *Adv. Opt. Mater.* **2022**, *10*, 2102722.
[75] L. K. Reb, M. A. Reus, M. Schwartzkopf, C. Rosemann, S. V. Roth, P. Müller-Buschbaum, The In-Situ GIXS Heuristic Tool for Efficient Reduction of 2D Grazing-Incidence Data. https://indico.frm2.tum.de/event/308/contributions/3031/attachments/696/1175/Abstract_DKG_2022_Lennart.pdf (24 January 2023).
[76] K. Momma, F. Izumi, *J. Appl. Crystallogr.* **2011**, *44*, 1272.